PHYSICAL REVIEW B **110**, 024424 (2024)

Editors' Suggestion

Spin wave dynamics excited by a focused laser pulse in antiferromagnet CrSBr

Huicong Liu and Ka Shen[*]

The Center for Advanced Quantum Studies and Department of Physics, Beijing Normal University, Beijing 100875, China and Key Laboratory of Multiscale Spin Physics, Ministry of Education, Beijing Normal University, Beijing 100875, China

(Received 29 April 2024; revised 26 June 2024; accepted 1 July 2024; published 17 July 2024)

The manipulation of magnetization dynamics by a focused laser with thermal and nonthermal mechanisms is a fascinating research topic. While such phenomena in ferromagnets have been intensively studied, the laser-induced magnetization dynamics in antiferromagnets remain to be clarified. In the present paper, we theoretically investigate both thermal and nonthermal mechanisms in CrSBr films, a van der Waals antiferromagnet with triaxial magnetic anisotropy, which has attracted great research interest recently. In contrast to previous reports on ferromagnet, the magnetization dynamics in CrSBr show several distinct features, especially for the thermal mechanism associated with the shear stress, where the presence and symmetry of spatial patterns of the dynamical magnetization strongly rely on the nonuniformity of shear stress and the strength of the in-plane magnetic field. From the nonthermal excitation, we find an isotropic spin-wave propagation at zero field, as well as an enhanced anisotropy introduced by the magnetic field. Our results could be useful for the laser-induced spin dynamics in antiferromagnets.

DOI: 10.1103/PhysRevB.110.024424

I. INTRODUCTION

Since the discovery of laser-induced ultrafast demagnetization [1], the manipulation of magnetism by a pulsed laser and the magnetization dynamics therein have become an attractive theme in the field of spintronics, where both nonthermal and thermal mechanisms are recognized to contribute. The nonthermal effects can be generated by either the transient magnetic field of the light [2–4] or an effective magnetic field due to photomagnetic interactions, which results in, for instance, the inverse Faraday effect (IFE) [5–7] and the inverse Cotton-Mouton effect [8]. For the thermal origin, the laser irradiates the sample and unavoidably causes an increase in the temperature of the sample. As a consequence, in rare-earth orthoferrites with strong temperature-dependent magnetic anisotropy, the magnetization dynamics can be triggered by the variation of the anisotropic field due to the ultrafast heating [9–11]. Another well-known thermal effect is a local stress introduced to the lattice by a focused laser beam, which generates sound waves and further excites spin waves or magnons via the spin-lattice coupling [12–15]. The interaction between sound and spin waves from this mechanism gives rise to various interesting phenomena, such as the bireflection of spin waves [16], the magnetization switching [17], the coherent oscillation between phonons and magnons [18], and the formation of spatial magnetization pattern [19].

The magnetization dynamics due to thermal and nonthermal origins of a focused laser can be distinguished from the distinct characteristics in the angular-dependent propagation of the generated spin waves [12,20,21], which can be read by the technique of all-optical spin-wave tomography, where the spin-wave dispersion and the coupling of magnon and phonon can be extracted [13,22,23]. As the early works in this direction mainly focused on ferro- and ferrimagnetic materials, the laser-induced magnetization dynamics in antiferromagnets have attracted arising attention [24–27]. For example, a quadrupolar shape of spin-wave propagation induced by laser was observed in a van der Waals antiferromagnetic CrSBr film [24,27], which may reflect the strong magnon-phonon coupling in this material [28–30]. An explicit theoretical analysis on laser-induced magnetization dynamics in antiferromagnets remains exclusive.

In the present paper, we study the laser-induced spin-wave dynamics in triaxial antiferromagnetic films, with representative materials CrSBr, by analyzing the spatiotemporal evolution of the measurable out-of-plane magnetization from both thermal and nonthermal mechanisms. For the thermal excitation, we consider the spin torques generated by pressure and shear stresses with both uniform and standing-wave profiles across the film thickness. In contrast to the pressure stress case, where the dynamical magnetization always presents quadrupolar spatial distribution, the shear stress is found to be able to excite magnetization dynamics only when the symmetry of the system is broken by an external magnetic field or by a nonuniform deformation across the thickness. In the case with an external magnetic field, the resulting spatial profile of dynamic magnetization follows the situation in ferromagnetic films, i.e., with a dipolar characteristic in spatial propagation of the excited spin wave. The shear stress with a standing-wave profile produces a quadrupolar shape of spin-wave propagation at zero field, which gradually gains the dipolar characteristic with applying and increasing the magnitude of the external magnetic field. In the nonthermal mechanism, we consider the IFE which causes isotropic spin wave propagation at zero field and shows anisotropic spin propagation in the presence of an external magnetic field.

---

[*] Contact author: kashen@bnu.edu.cn

II. MAGNETOSTATIC SPIN WAVES IN ANTIFERROMAGNET

According to Refs. [24,27–30], the intrasublattice exchange interaction for the magnetic moments within a single layer in CrSBr is sufficiently strong to form the ferromagnetic layer and the weak intersublattice between neighboring layers is responsible for the establishment of the interlayer antiferromagnetic order. Since the strong intrasublattice is irrelevant to the film geometry in the sub-Terahertz frequency scale, we consider a two-sublattice antiferromagnetic model and take the total energy density consisting of the Zeeman energy, a triaxial anisotropic term, and an intersublattice exchange coupling as

$$\begin{aligned}\mathcal{E}(\mathbf{r}, z, t) = &- \mu_0 \mathbf{H} \cdot \sum_{i=1,2} M_0 \mathbf{m}_i + 2\mathcal{J} \mathbf{m}_1 \cdot \mathbf{m}_2 \\ &- \sum_{i=1,2} \sum_{\eta=x,y} K^\eta \left(m_i^\eta\right)^2,\end{aligned} \tag{1}$$

where $\mathbf{m}_i(\mathbf{r}, z, t)$ stands for the normalized magnetization of the ith sublattice with $\mathbf{r}$ and z being the in-plane and out-of-plane components of the position vector. M_0 is the sublattice saturation magnetization. By including both the external magnetic field $\mathbf{H}_0$ (along the x direction) and the demagnetization contribution $\mathbf{H}_{\text{in}}$, the total magnetic field is expressed as $\mathbf{H}(\mathbf{r}, t) = \mathbf{H}_0 + \mathbf{H}_{\text{in}}(\mathbf{r}, t)$. $\mathcal{J}$ and K^η are the coefficients of the Heisenberg exchange interaction and the anisotropy, respectively, with their values $\mathcal{J} > 0$ and $K^x > K^y > 0$. As a van der Waals antiferromagnet with in-plane easy-axis anisotropy, the magnetic moments of exfoliated CrSBr are naturally aligned within the plane, which is therefore suitable for observing the dynamics of the out-of-plane magnetization by optical approaches. For other antiferromagnets with bulk crystalline, a proper crystal face orientation is required to make the magnetic moments within the film plane. In addition, the weak antiferromagnetic exchange interaction between ferromagnetic layers in CrSBr with opposite spins makes the anisotropy and dipolar interaction more important than those in normal antiferromagnets. Assuming that the external magnetic field is weaker than the spin-flop field, the system is in the collinear configuration with Néel vector along the x direction. The magnetization dynamics of the two sublattices can be described by the Landau-Lifshitz equation

$$\partial_t \mathbf{m}_{1(2)} = -\gamma \mathbf{m}_{1(2)} \times \mu_0 \mathbf{H}_{\text{eff},1(2)}, \tag{2}$$

where γ is the gyromagnetic ratio and $\mu_0 \mathbf{H}_{\text{eff},1(2)} = -\nabla_{\mathbf{m}_{1(2)}} \mathcal{E}/M_0$ calculated from Eq. (1) represents the total effective magnetic field acting on the local sublattice magnetization. By substituting the time-harmonic solution into Eq. (2), we find the relation between the dynamical magnetization components and the demagnetization field within the magnetic film as

$$\begin{aligned} m_{1(2)}^y &= \mu_0(\kappa_{1(2)} H_{\text{in},y} + i\nu_{1(2)} H_{\text{in},z}), \\ m_{1(2)}^z &= -i\mu_0(\kappa'_{1(2)} H_{\text{in},y} + i\nu'_{1(2)} H_{\text{in},z}), \end{aligned} \tag{3}$$

where the expressions of the coefficients κ_i, κ'_i, ν_i, and ν'_i are shown in Appendix A. Then, by following the standard approach for magnetostatic spin waves [31], we express the demagnetization field by the gradient of a scalar potential, i.e., $\mathbf{H}_{\text{in}} = \nabla\phi$, and solve the boundary condition of the scalar potential in the film geometry associated with the Maxwell's equation $\nabla \cdot [M_0(\mathbf{m}_1 + \mathbf{m}_2) + \mathbf{H}_{\text{in}}] = 0$. The characteristic equation of the eigenfrequencies for a given in-plane wave vector $\mathbf{k}$ can be expressed as [32,33]

$$\begin{aligned}&(1+\kappa')^2 \left(\frac{k_{\text{in}}^z}{k}\right)^2 - 2(1+\kappa') \cot\left(k_{\text{in}}^z d\right) \frac{k_{\text{in}}^z}{k} - 1 \\ &\quad = -(\nu')^2 \sin^2\theta_{\mathbf{k}},\end{aligned} \tag{4}$$

where d represents the film thickness and $\theta_{\mathbf{k}}$ is the angle between the wave vector and the Néel vector. The normal component of the wave vector k_{in}^z satisfies

$$\left(k_{\text{in}}^z\right)^2 = -\frac{1 + \kappa \sin^2\theta_{\mathbf{k}}}{1+\kappa'} k^2. \tag{5}$$

Here, κ, κ', and ν' are functions of ω, as shown in Appendix A. The numerical solution of Eq. (4) leads to a series of eigenfrequencies for the spin waves, $\omega_{j\mathbf{k}}$, of which the corresponding wave functions are given by

$$\mathcal{M}_{1(2),j}^y(\mathbf{k}, z) = -i\mu_0 C_{j\mathbf{k}}\left(\kappa_{1(2)} k \sin\theta_{\mathbf{k}} Z_1 + \nu_{1(2)} k_{\text{in}}^z Z_2\right), \tag{6}$$

$$\mathcal{M}_{1(2),j}^z(\mathbf{k}, z) = -\mu_0 C_{j\mathbf{k}}\left(\nu'_{1(2)} k \sin\theta_{\mathbf{k}} Z_1 + \kappa'_{1(2)} k_{\text{in}}^z Z_2\right), \tag{7}$$

with $Z_1(z) = \sin(k_{\text{in}}^z z)$ and $Z_2(z) = \cos(k_{\text{in}}^z z)$. The common coefficient C_j in Eqs. (6) and (7) is determined by the orthonormality condition [34]

$$\sum_{i=1,2} (-1)^i \int_{-d/2}^{d/2} dz \left(\mathcal{M}_{i,j}^{z*} \mathcal{M}_{i,j'}^y - \mathcal{M}_{i,j}^{y*} \mathcal{M}_{i,j'}^z\right) = i\delta_{jj'}, \tag{8}$$

in which $\delta_{jj'}$ stands for the Kronecker delta function.

III. SPIN-WAVE DYNAMICS EXCITED BY A FOCUSED LASER PULSE

According to the linear response theory, the dynamical magnetization can be described, in general, by

$$\mathbf{m}(\mathbf{r}, z, t) = \frac{1}{M_0} \int d\mathbf{r}' dz' dt' \boldsymbol{\chi}(\mathbf{r}, z, t; \mathbf{r}', z', t') \cdot \mathbf{H}_T(\mathbf{r}', z', t'), \tag{9}$$

where $\boldsymbol{\chi}$ is the response tensor and $\mathbf{H}_T$ is the perturbation field triggering the magnetization dynamics. By projecting Eq. (9) into the eigenmodes of the spin waves, the spatiotemporal evolution of the induced transverse magnetization components in the ith sublattice can be written as [21]

$$\begin{aligned} m_i^\alpha(\mathbf{r}, z, t) = &\sum_{\mathbf{k}} e^{i\mathbf{k}\cdot\mathbf{r}} \frac{1}{M_0} \int dz' dt' \\ &\times \sum_{\beta, i'} \chi_{ii'}^{\alpha\beta}(\mathbf{k}, z, z', t, t') H_{i'T}^\beta(\mathbf{k}, z', t'), \end{aligned} \tag{10}$$

with $\alpha, \beta \in \{y, z\}$. The spin susceptibility $\chi_{ii'}^{\alpha\beta}$ is given by

$$\begin{aligned} \chi_{ii'}^{\alpha\beta}(\mathbf{k}, z, z', t, t') = &-i\gamma\mu_0 M_0 \sum_j e^{-i\omega_{j\mathbf{k}}(t-t')} \\ &\times \mathcal{M}_{i,j}^\alpha(\mathbf{k}, z) \mathcal{M}_{i',j}^{\beta*}(\mathbf{k}, z'). \end{aligned} \tag{11}$$

The dissipation effect can be included by introducing $(1 - i\alpha_0)$ in front of $\omega_{j\mathbf{k}}$, with α_0 denoting the Gilbert

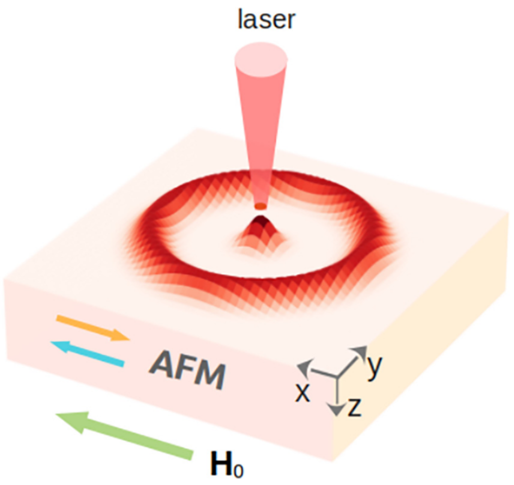

FIG. 1. The schematic of our geometry with the the upper and lower surfaces of the magnetic film defined as $z = -d/2$ and $d/2$, respectively. The equilibrium sublattice magnetic moments and the external magnetic field both lie in the x-direction within the film plane. A focused laser pulse heats the film and generates a local lattice deformation at the heating area as well as a propagating elastic wave (the ring-shaped deformation).

damping constant. The out-of-plane component of the net magnetization m_{net}^z integrated over the magnetic film can be characterized experimentally by the Faraday (Kerr) angle Θ_{F} as

$$\Theta_F(\mathbf{r}, t) \propto \sum_{\mathbf{k}} e^{i\mathbf{k}\cdot\mathbf{r}} \sum_j \overline{m_{\text{net},j}^z(\mathbf{k}, t)}, \tag{12}$$

where the contribution from the jth spin wave mode with the wave vector $\mathbf{k}$ is derived from Eq. (10), that is, $\overline{m_{\text{net},j}^z(\mathbf{k}, t)} = \int_{-d/2}^{d/2} (m_{1,j}^z + m_{2,j}^z)(\mathbf{k}, z, t) dz$.

A. Thermal excitation

To simulate the thermal excitation of spin waves by a focused laser pulse, we model the perturbation field $\mathbf{H}_T$ in Eq. (10) by considering the lattice deformation due to local heating schematically shown in Fig. 1. The thermal expansion due to the heating effect generates shear and pressure stresses to the lattice, which brings in not only a static lattice deformation at the heating area but also sonic pulses propagating with approximately transverse or longitudinal sound speed. The lattice deformation further creates a torque to the magnetization due to the magnetoelastic coupling [20,21]. In contrast to the ferromagnetic case, the magnetoelastic coupling mainly correlates the lattice with the Néel vector, instead of the net magnetization. Its explicit form in the long-wavelength limit reads [35]

$$\mathcal{H}_{\text{me}} = B^{\alpha\beta} n^\alpha n^\beta e^{\alpha\beta}, \tag{13}$$

where $B^{\alpha\beta} = B^{\parallel}\delta^{\alpha\beta} + B^{\perp}(1 - \delta^{\alpha\beta})$ are the magnetoelastic coupling constants, $n^\alpha \simeq (m_1^\alpha - m_2^\alpha)/2$ is the α component of the Néel vector, and $e^{\alpha\beta} = (\partial_\beta R_\alpha + \partial_\alpha R_\beta)/2$ corresponds to the strain of the lattice.

By considering the fact that the lattice deformations due to the shear and pressure stresses are mainly in the out-of-plane and in-plane directions separately with a relatively weak coupling, we neglect the interplay between the in-plane and out-of-plane lattice dynamics for the simplification of our analytical description. Since the resulting sonic pulse propagates separately with the transverse and longitudinal sound speeds, the out-of-plane and in-plane lattice deformation are described by $\mathbf{R}_z(\mathbf{r}, z, t)$ and $\mathbf{R}_l(\mathbf{r}, z, t)$, respectively [20,21]. To analyze the role of the different profiles of the displacement in the thickness direction, we take $\mathbf{R}_l \simeq \mathbf{g}_l(\mathbf{r}, t) f_l(z)$ and $\mathbf{R}_z \simeq g_z(\mathbf{r}, t) f_z(z)\mathbf{e}_z$. The $\mathbf{g}_l(\mathbf{r}, t)$ and $g_z(\mathbf{r}, t)\mathbf{e}_z$ including both localized deformation and acoustic pulses can be obtained through the equations of lattice motion with the temperature distribution [21]. For the profiles of the displacements in the thickness direction, we take two cases in the following: (1) Uniform profile $f_{z(l)}^{\text{u}}(z) = 1$ [21] and (2) standing-wave form $f_{z(l)}^{\text{st}}(z) = \cos(k_{\text{p}}^z(z + d/2))$ with $k_{\text{p}}^z = \pi/2d$, which corresponds to a free boundary of the upper surface $z = -d/2$ and a fixed boundary of the lower surface $z = d/2$ [36–38]. Both cases are considered to be relevant to the recent experiments in van der Waals antiferromagnets like CrSBr [24,25,27].

The effective excited magnetic field $\mu_0\mathbf{H}_{iT} = -\boldsymbol{\nabla}_{\mathbf{m}_i}\mathcal{H}_{\text{me}}/M_0$ from the magnetoelastic coupling reads

$$\boldsymbol{H}_{1T} = -\boldsymbol{H}_{2T} = -\frac{B^{\perp}}{2\mu_0 M_0} ik(R_l \sin 2\theta_{\boldsymbol{k}} \boldsymbol{e}_y + R_z \cos\theta_{\boldsymbol{k}} \boldsymbol{e}_z). \tag{14}$$

Substituting it into the Eq. (10), we can get $\overline{m_{\text{net},j}^z(\mathbf{k}, t)}$ from the pressure stress,

$$\overline{m_{\text{net},j}^z(\mathbf{k}, t)} \propto -k^2 e^{-\frac{k^2W^2}{4}} \sin 2\theta_{\mathbf{k}} \frac{M_j^{\text{pr}}(\mathbf{k})}{\left(\omega_{\text{p}}^{\text{pr}}\right)^2} \times \left[A_{\mathbf{k}}^{\text{pr}} e^{-i\omega_{j\mathbf{k}}t} + B_{\mathbf{k}}^{\text{pr}} e^{-i\omega_{\text{p}}^{\text{pr}}t} + C_{\mathbf{k}}^{\text{pr}} e^{i\omega_{\text{p}}^{\text{pr}}t} - \frac{1}{\omega_{j\mathbf{k}}}\right], \tag{15}$$

and that from the shear stress

$$\overline{m_{\text{net},j}^z(\mathbf{k}, t)} \propto -ik^3 e^{-\frac{k^2W^2}{4}} \cos\theta_{\mathbf{k}} \frac{M_j^{\text{sh}}(\mathbf{k})}{\left(\omega_{\text{p}}^{\text{sh}}\right)^2} \times \left[A_{\mathbf{k}}^{\text{sh}} e^{-i\omega_{j\mathbf{k}}t} + B_{\mathbf{k}}^{\text{sh}} e^{-i\omega_{\text{p}}^{\text{sh}}t} + C_{\mathbf{k}}^{\text{sh}} e^{i\omega_{\text{p}}^{\text{sh}}t} - \frac{1}{\omega_{j\mathbf{k}}}\right], \tag{16}$$

where

$$A_{\mathbf{k}}^{\text{pr(sh)}} = \frac{1}{\omega_{j\mathbf{k}}} - B_{\mathbf{k}}^{\text{pr(sh)}} - C_{\mathbf{k}}^{\text{pr(sh)}}, \tag{17}$$

$$B_{\mathbf{k}}^{\text{pr(sh)}} = \frac{1}{2\left(\omega_{j\mathbf{k}} - \omega_{\text{p}}^{\text{pr(sh)}}\right)}, \tag{18}$$

$$C_{\mathbf{k}}^{\text{pr(sh)}} = \frac{1}{2\left(\omega_{j\mathbf{k}} + \omega_{\text{p}}^{\text{pr(sh)}}\right)}. \tag{19}$$

Here, the frequency $\omega_{\text{p}}^{\text{pr}}$ from $\mathbf{R}_l$ lattice displacement is $\omega_{\text{p}}^{\text{pr}} = \sqrt{c_l^2k^2 + (c_tk_{\text{p}}^z)^2}$ and the frequency $\omega_{\text{p}}^{\text{sh}}$ due to the dynamic of $\mathbf{R}_z$ is $\omega_{\text{p}}^{\text{sh}} = \sqrt{c_t^2k^2 + (c_lk_{\text{p}}^z)^2}$, with c_t and c_l being the transverse and longitudinal sound velocities. W characterizes the size of the laser spot. The expressions of $M_j^{\text{pr}}(\mathbf{k})$ and $M_j^{\text{sh}}(\mathbf{k})$

are given by

$$M_j^{\mathrm{pr}}(\mathbf{k}) = \overline{\mathcal{M}_j^z(\mathbf{k})} \times \overline{\left(\mathcal{N}_j^y(\mathbf{k})\right)^* f_l(z)} \tag{20}$$

and

$$M_j^{\mathrm{sh}}(\mathbf{k}) = \overline{\mathcal{M}_j^z(\mathbf{k})} \times \overline{\left(\mathcal{N}_j^z(\mathbf{k})\right)^* f_z(z)}, \tag{21}$$

where $\boldsymbol{\mathcal{M}}_j = \boldsymbol{\mathcal{M}}_{1,j} + \boldsymbol{\mathcal{M}}_{2,j}$ and $\boldsymbol{\mathcal{N}}_j = \boldsymbol{\mathcal{M}}_{1,j} - \boldsymbol{\mathcal{M}}_{2,j}$ represent the magnetization and the Néel vector for the jth eigenmode of the magnetostatic spin wave, respectively, and the overline notation above a function stands for an integral over the thickness, for instance, $\overline{\mathcal{M}_j^z} = \int_{-d/2}^{d/2} \mathcal{M}_j^z dz$, where the symmetry of the wave functions is essential to give a finite value.

B. Nonthermal excitation

For the nonthermal excitation mechanism, we consider the IFE of a circularly polarized laser pulse [39,40], which results in a strong magnetic field pulse along the direction of laser beam [5–7]. The circularly polarized laser beam is set to propagate within the z direction, so the effective magnetic field from IFE is

$$\mathbf{H}_T(\mathbf{r}, t) = e^{-r^2/W^2} \delta(t) \tau_{\mathrm{d}} h_z \boldsymbol{e}_z, \tag{22}$$

where h_z is the amplitude of the effective excited field and τ_{d} stands for the duration of the pulse. By substituting Eq. (22) into Eq. (10), we obtain the z component of the induced sublattice magnetization as

$$\overline{m_{\mathrm{net},j}^z(\mathbf{k}, t)} \propto -ie^{-\frac{k^2W^2}{4}} e^{-i\omega_{j\mathbf{k}}t} \overline{\mathcal{M}_j^z(\mathbf{k})} \times \overline{\left(\mathcal{M}_j^z(\mathbf{k})\right)^*} h_z. \tag{23}$$

IV. RESULTS

In this section, we apply our formalism to CrSBr, a representative antiferromagnetic van der Waals material with triaxial anisotropy. In the geometry of Fig. 1, we take the material parameters $\mu_0 H_{\mathrm{ex}} = 0.2\,\mathrm{T}$, $\mu_0 H_{\mathrm{a}}^x = 1.6\,\mathrm{T}$, $\mu_0 H_{\mathrm{a}}^y = 0.64\,\mathrm{T}$, $\mu_0 M_0 = 0.26\,\mathrm{T}$ [24,25], and the transverse and longitudinal sound velocities $c_t = 1.1\,\mathrm{km}/s$ and $c_l = 5\,\mathrm{km}/s$ [41]. The damping constant is adopted to be $\alpha_0 = 0.1$. The thickness and size of the laser spot are taken to be $d = 150\,\mathrm{nm}$ and $W = 1.4\,\mu\mathrm{m}$, respectively. Note that although the strength of the Heisenberg exchange interaction is even weaker than the anisotropy, it is still important to include it for the proper magnon spectrum [24,25].

A. Thermal excitation with uniform deformation in thickness direction

The results of the thermal excitation from the calculation with an acoustic wave distributed uniformly in the thickness direction, i.e., with $f_{z(l)}^{\mathrm{u}}(z) = 1$, are plotted in Fig. 2, which displays the snapshots of the $\overline{m_{\mathrm{net}}^z}$ distribution with arbitrary unit at 4 ns after laser pumping at zero magnetic field. A quantitative estimation of $\overline{m_{\mathrm{net}}^z}$ requires not only the laser intensity but also various materials parameters, such as the magnetoelastic coupling coefficient and thermal expansion coefficient for thermal excitation, and the magneto-optic susceptibility for nonthermal mechanism. By considering the fact that the experimental measurement in CrSBr has already shown the detectable magnitude in the magneto-optical Kerr effect according to Ref. [27], we here focus on the spatiotemporal evolution of the signal. As shown by Fig. 2(a), the $\overline{m_{\mathrm{net}}^z}$ dynamics can be efficiently excited by the pressure stress, which presents very similar features to those in the ferromagnetic case, namely, with a quadrupolar around the heating area and an expansive circle due to the propagating of a sonic pulse [21]. The excitation due to shear stress is, however, forbidden according to Fig. 2(b), which is in sharp contrast to the situation in ferromagnets [21].

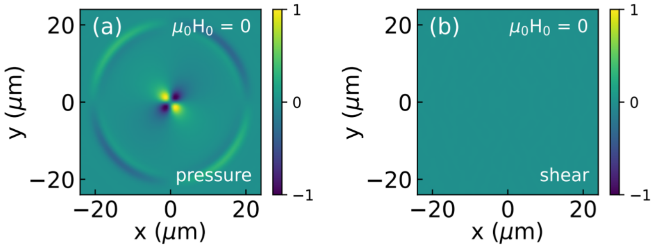

FIG. 2. Snapshot of $\overline{m_{\mathrm{net}}^z}$ distribution (in arbitrary units) due to (a) the pressure stress and (b) the shear stress in CrSBr at 4 ns after an ultrafast laser pulse in the absence of external magnetic field.

To understand the vanishing of the net magnetization $\overline{m_{\mathrm{net}}^z}$ in the shear-stress-induced dynamics in Fig. 2(b), we analyze the properties of the zero-field magnon dispersion relations and the symmetry of the corresponding wave functions. The typical features of the magnon dispersion are explicitly shown as Fig. 3(a) by taking $\theta_{\mathbf{k}} = \pi/3$ as an example, where the blue and cyan curves correspond to the high- and low-frequency sets of the volume modes, labeled VHs and VLs in the following. The orange curve and the pink one within the gap between VHs and VLs are two surface modes [33]. The one of the higher (lower) frequency are labeled as SH (SL). More results with different $\theta_{\mathbf{k}}$ can be found in Appendix B.

Figures 3(b) and 3(c) plot the spatial profiles of the magnetization density $\mathcal{M}_j^z$ and the Néel density $\mathcal{N}_j^z$ along the thickness direction for two selected volume modes VH$_1$ and VL$_1$, as well as the two surface modes at the wave vectors indicated by the black dots in Fig. 3(a). As one can see from Fig. 3(b), the profiles of $\mathcal{M}_j^z$ for VH$_1$ and SL are antisymmetric functions, resulting in $\overline{\mathcal{M}_j^z} = 0$ and hence a vanishing contribution to M_j^{sh} according to Eq. (21). For VL$_1$ and SH, their symmetric profile of $\mathcal{M}_j^z$ in Fig. 3(b) gives a finite average value of $\overline{\mathcal{M}_j^z}$. However, as shown in Fig. 3(d), their profiles of $\mathcal{N}_j^z$ are antisymmetric, which leads to $\overline{\mathcal{N}_j^z f_z(z)} = 0$ under the condition of a uniform lattice deformation profile $f_z^{\mathrm{u}}(z) = 1$. As a consequence, these modes do not contribute to $M_j^{\mathrm{sh}}(\mathbf{k})$ neither. A systematic examination shows that all VHs (VLs) exhibit the same symmetry as VH$_1$ (VL$_1$), which thus indicates a zero $M_j^{\mathrm{sh}}(\mathbf{k})$ for any mode in the absence of an external magnetic field. This explains the absence of the magnetization dynamics in Fig. 2(b). In the meantime, the symmetric profiles of $\mathcal{N}_j^y$ and $\mathcal{M}_j^z$ for the VLs and SH give nonvanishing $M_j^{\mathrm{pr}}(\mathbf{k})$ in Eq. (20), forming the snapshot of $\overline{m_{\mathrm{net}}^z}$ in Fig. 2(a).

For a comparison, we calculate the dispersion curves and the typical wave functions at the same angle $\theta_{\mathbf{k}} = \pi/3$ in the

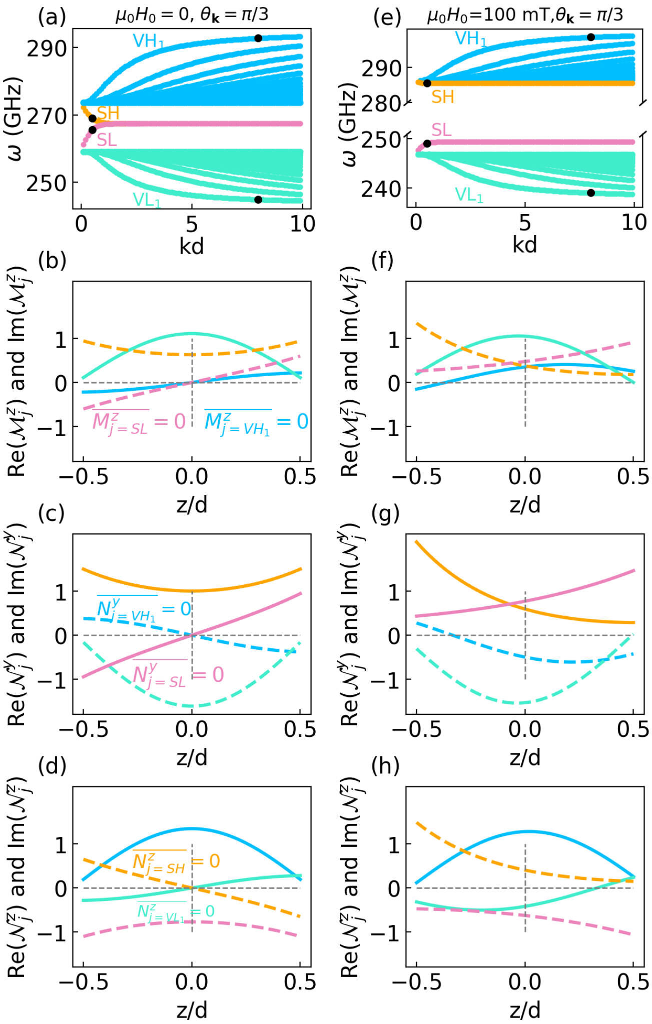

FIG. 3. Spin-wave dispersion relations of CrSBr at $\theta_{\mathbf{k}} = \pi/3$ (a) without and (b) with an external magnetic field at 100 mT. Blue and cyan curves represent the high- and lower-frequency sets of volume modes, i.e., VHs and VLs, while the orange and pink curves correspond to the dispersions of the two surface modes (SH and SL) [33]. Spatial profiles of wave functions $\mathcal{M}_j^z$, $\mathcal{N}_j^y$, and $\mathcal{N}_j^z$ at (b)–(d) 0 mT and (f)–(h) 100 mT, for the modes indicated in (a) and (b), i.e., VH$_1$ and VL$_1$ at $kd = 8$ and SH and SL at $kd = 0.5$. The colored solid (dashed) curves stand for the nonzero real (imaginary) part of wave functions with those vanishing components discarded.

presence of a magnetic field at $\mu_0 H_0 = 100$ mT, as plotted in Figs. 3(e)–3(h). The magnetic field along the Néel's direction not only introduces a frequency shift of each magnon band but also breaks the symmetry of the wave functions. As clearly seen from Figs. 3(f)–3(h), neither $\mathcal{M}_j^z$ nor $\mathcal{N}_j^z$ varies asymmetrically in the thickness direction. This implies finite values of $\overline{\mathcal{M}_j^z}$ and $\overline{\mathcal{N}_j^z f_z^{\rm u}(z)}$, resulting in a nonvanishing $M_j^{\rm sh}$. One may expect the activation of the shear-stress-induced magnetization dynamics. Indeed, by evaluating $M_j^{\rm sh}$ of different modes and substituting them into Eqs. (12) and (16), we do observe the spatiotemporal evolution of the magnetization, as shown in Fig. 4 with a magnetic field $\mu_0 H_0 = 100$ mT, where the expansions of the activated area are observed and similar to that in a ferromagnetic film generated by the same mechanism [20,21]. This can be understood by the fact that the magnetic field along the Néel direction breaks the time-reversal symmetry of the antiferromagnetic system and makes it analogous to a ferromagnet in terms of spin-wave excitation.

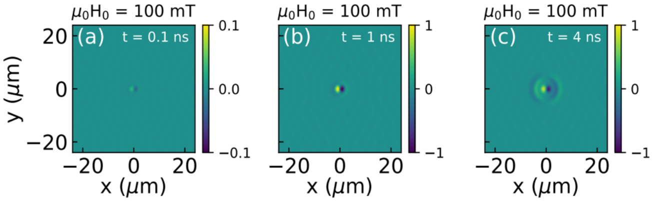

FIG. 4. Snapshot of $\overline{m^z_{\rm net}}$ distribution (in arbitrary units) due to shear stress in CrSBr with 100 mT external magnetic field at (a) $t = 0.1$ ns, (b) $t = 1$ ns, and (c) $t = 4$ ns after the arrival of the laser pulse.

B. Thermal excitation with standing-wave profile in thickness direction

The thermal excitation with a standing sound wave in the thickness direction, i.e., with $f^{\rm st}_{z(l)}(z) = \cos(k_{\rm p}^z(z + d/2))$ as explained in Sec. III A, is then studied. The results with zero magnetic field are plotted in Fig. 5, which displays the snapshots of the $\overline{m^z_{\rm net}}$ distribution at 4 ns after the sudden heating due to the laser pulse.

As we can see, both pressure and shear stresses can generate magnetization dynamics without a magnetic field. This is because the applied $f^{\rm st}_{z(l)}$ without even or odd symmetry always gives finite $\overline{\mathcal{N}_j^y f_l^{\rm st}(z)}$ and $\overline{\mathcal{N}_j^z f_z^{\rm st}(z)}$ in Eqs. (20) and (21). One distinct feature, compared to the situation with a uniform profile in Fig. 4, the circular-shaped expansion of the signal disappears in the snapshot of $\overline{m^z_{\rm net}}$ induced by shear stress in the present case, which suggests the significant suppression

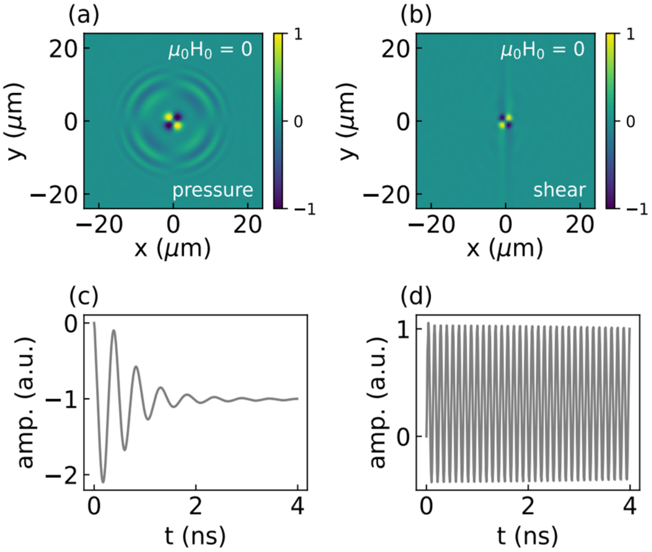

FIG. 5. Snapshot of $\overline{m^z_{\rm net}}$ at 4 ns induced by (a) pressure stress and (b) shear stress with a standing-wave acoustic profile $f^{\rm st}_{z(l)}(z) = \cos(k_{\rm p}^z(z + d/2))$ in the absence of magnetic field. The temporal evolution of $\overline{m^z_{\rm net}}$ induced by (c) pressure stress and (d) shear stress at position $x = 1$ μm and $y = 1$ μm.

of the propagating sonic pulse. This can be understood as follows. According to Eq. (16), the size of the laser spot determines the amplitudes of the activated spin waves by the factor $e^{-k^2W^2/4}$, which indicates that the dominance of the modes with a wave vector $k < 2/W$. From the condition $W \gg d$, we have $k_p^z = 2\pi/d \gg k$, which leads to $\omega_{\rm p}^{\rm sh} \simeq c_l k_p^z + (c_t k)^2/(2c_l k_p^z)$. The lateral velocity of the sonic pulses is estimated to be $\partial_k \omega_{\rm p}^{\rm sh} = c_t^2 k/(c_l k_p^z) \ll c_t$, explaining the vanishing of the propagation in Fig. 5(b). This picture is also supported by a simulation at a longer time with $t = 120$ ns, where the circular expansion of the shear sonic pulse becomes visible again (not shown). For the pressure-induced dynamics, we have $\omega_{\rm p}^{\rm pr} \simeq c_t k_p^z + (c_l k)^2/2c_t k_p^z$ and hence $\partial_k \omega_{\rm p}^{\rm pr} \approx 0.57 c_l$, which is sufficient to maintain the circular-shaped propagating profile in Fig. 5(a).

To show the temporal evolution of $\overline{m^z_{\rm net}}$ in the exposure area, we present the results as a function of time at the position with $x = 1$ μm and $y = 1$ μm in Figs. 5(c) and 5(d). The $\overline{m^z_{\rm net}}$ induced by pressure and shear stresses both exhibit oscillatory behavior, but with different frequencies about 13 GHz and 52 GHz, respectively. These frequencies correspond to $\omega_{\rm p}^{\rm pr} \simeq c_t k_p^z$ and $\omega_{\rm p}^{\rm sh} \simeq c_l k_p^z$. The irrelevance of the spin-wave frequencies $\omega_{j\mathbf{k}}$ is due to the small magnitude of $A_{\mathbf{k}}^{\rm pr(sh)}$ in Eqs. (15) and (16) under the condition of $\omega_{j\mathbf{k}} \gg \omega_{\rm p}^{\rm pr(sh)}$, according to Eqs. (17)–(19). The relatively quick decay of the oscillation amplitude in Fig. 5(c) reflects the faster propagation of the pressure pulse discussed above, leaving a static nonzero quadrupolar at the exposure area.

Another surprising feature in Fig. 5 is that the spatial distribution of $\overline{m^z_{\rm net}}$ in the exposure area generated by the shear stress looks quite similar to that due to the pressure stress, namely, with quadrupolar symmetry. This differs from previous reports of ferromagnets [12,20] and the results of antiferromagnets with a uniform deformation shown in Fig. 4. Note that the spatial profile of the dynamical magnetization distribution, as a superposition of spin waves with different wave vectors, is determined by the wave-function properties of different modes. As expressed by Eq. (15), the spatial symmetry of $\overline{m^z_{\rm net}}$ induced by pressure stress is related to the $M_j^{\rm pr}(\mathbf{k})$ and the factor $\sin 2\theta_{\mathbf{k}}$ from the anisotropic magnetoelastic coupling. A detailed analysis shows that the contributed VLs and SH modes (of nonvanishing $\overline{\mathcal{M}_j^z}$) with $\theta_{\mathbf{k}} = \theta_0$, $\pi - \theta_0$, $\pi + \theta_0$, and $2\pi - \theta_0$, which share the same dispersion relations, also have the same spatial profiles of $\mathcal{M}_j^z$ and $\mathcal{N}^y_{j,\rm st} = \mathcal{N}^y_j f_l^{\rm st}$. As an example, the results of $\mathcal{N}^y_{j,\rm st}$ with $\theta_0 = \pi/3$ are presented in Figs. 6(a)–6(d), with the corresponding $\mathcal{M}_j^z$ the same as Fig. 2(b). As a consequence, $\overline{m^z_{\rm net}}$ exhibits a quadrupolar symmetry determined by the factor $\sin 2\theta_{\mathbf{k}}$. For the shear-stress-induced mechanism, however, $\mathcal{N}^z_{j,\rm st}$ with $\theta_{\mathbf{k}} = \theta_0$ and $\pi + \theta_0$ for VLs and SH present an opposite sign to those with $\theta_{\mathbf{k}} = \pi - \theta_0$ and $2\pi - \theta_0$ according to Figs. 6(e)–6(h) with $\theta_0 = \pi/3$, which, together with the angular dependence $\cos\theta_{\mathbf{k}}$ in Eq. (16), also results in a quadrupolar characteristic.

As shown in Fig. 3, an external magnetic field along the easy axis could significantly modify the symmetry of the wave functions. It is thus necessary to examine the role of the magnetic field in the present case. The profiles of $\mathcal{M}_j^z$, $\mathcal{N}^y_{j,\rm st}$ $\mathcal{N}^z_{j,\rm st}$ at 100 mT with $\theta_0 = \pi/3$ are plotted in Fig. 7. As seen, the profiles of $\mathcal{M}^z_{j,\rm st}$ from the four $\theta_{\mathbf{k}}$ in Figs. 7(a)–7(d) all share the same shape for each mode, except a reversal with respect to the $z = 0$ plane, which thus give the same value of $\overline{\mathcal{M}^z_{j,\rm st}}$. For $\mathcal{N}^y_{j,\rm st}$ in Figs. 7(e)–7(h) and $\mathcal{N}^z_{j,\rm st}$ in Figs. 7(i)–7(l), although their details at the four angles still show some differences, the integral over the thickness $\overline{\mathcal{N}^y_{j,\rm st}}$ and $\overline{\mathcal{N}^z_{j,\rm st}}$ leads to the same sign for each mode. As a consequence, one may expect that the symmetry of $\overline{m^z_{\rm net}}$ induced by pressure and shear stresses should be determined mainly by the factors $\sin 2\theta_{\mathbf{k}}$ and $\cos\theta_{\mathbf{k}}$, respectively, under a large magnetic field. This is confirmed by direct calculations of spatial magnetization distribution, from which the results are plotted in Fig. 8, where quadrupolar and dipolar features are clearly

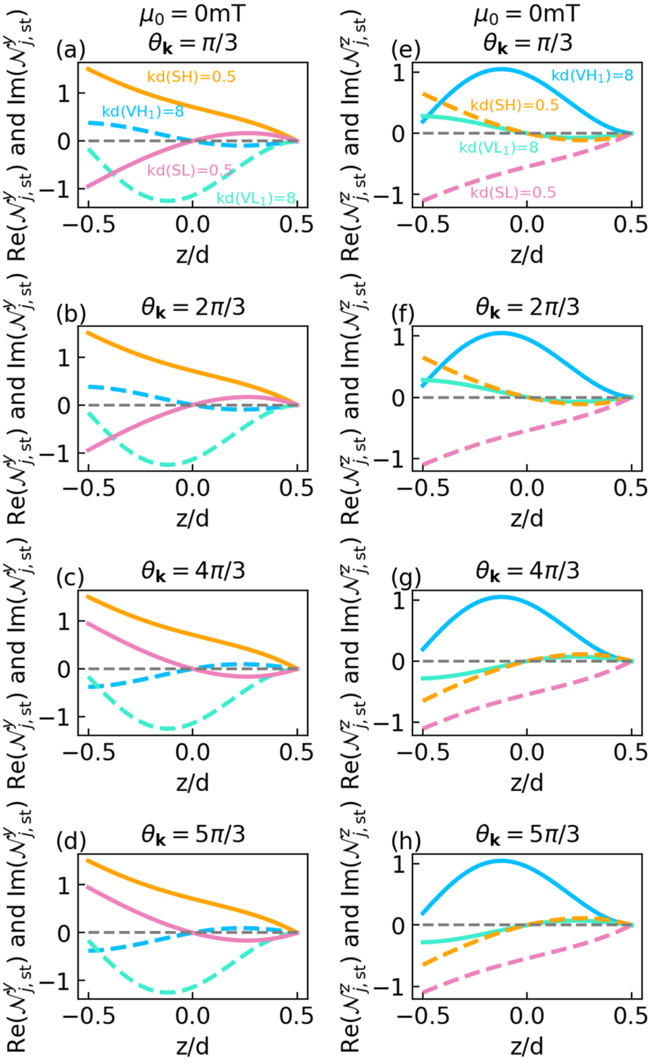

FIG. 6. Zero-field spatial profiles of (a)–(d) $\mathcal{N}^y_{j,\rm st} = \mathcal{N}^y_{j,st} f_l^{\rm st}$ and (e)–(h) $\mathcal{N}^z_{j,\rm st} = \mathcal{N}^z_{j,st} f_z^{\rm st}$ in the thickness direction for the selected SH and SL modes at $kd = 0.5$ and VH$_1$ and VL$_1$ modes at $kd = 8$. Here, we take $\theta_{\mathbf{k}} = \pi/3$, $2\pi/3$, $4\pi/3$, $5\pi/3$. The meanings of the colored curves are all the same as those in Fig. 3.

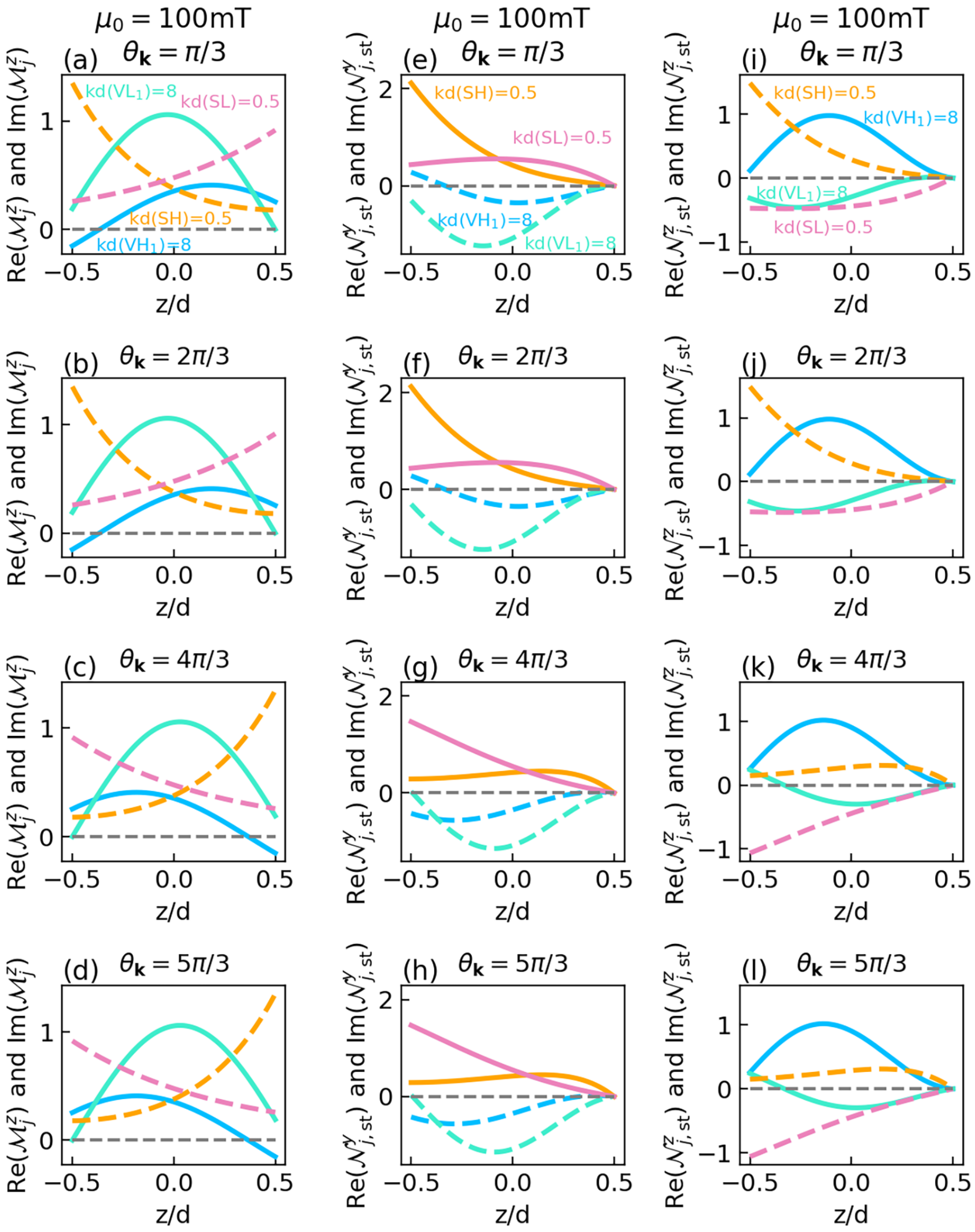

FIG. 7. Spatial profiles of (a)–(d) $\mathcal{M}_j^z$, (e)–(h) $\mathcal{N}_{j,\mathrm{st}}^y = \mathcal{N}_j^y f_z^{\mathrm{st}}$, and (i)–(l) $\mathcal{N}_{j,\mathrm{st}}^z = \mathcal{N}_j^z f_z^{\mathrm{st}}$ for selected SH and SL modes at $kd = 0.5$ and VH$_1$ and VL$_1$ modes at $kd = 8$ with an external magnetic field $\mu_0 H_0 = 100$ mT. All curves have the same meanings as those in Fig. 3.

recognizable from the spin-wave excitation due to the pressure and shear stresses.

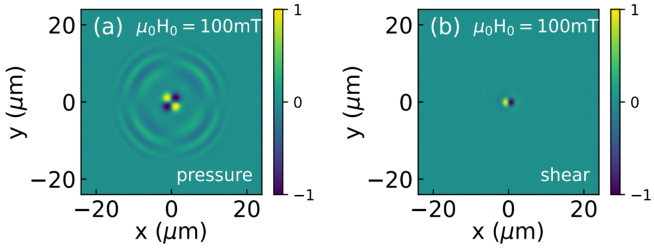

FIG. 8. Snapshot of $\overline{m_{\mathrm{net}}^z}$ distribution (in arbitrary units) at 4 ns due to (a) pressure stress and (b) shear stress with $\mu_0 H_0 = 100$ mT.

C. Nonthermal excitation

In the nonthermal excitation, the dynamic evolution of magnetization without and with an external magnetic field (100 mT) is shown in Fig. 9, where we have assumed that the rotation of the magnetic moments after the IFE effective field pulse is small enough to make the system lie in the linear spin-wave regime. At an early time $t = 0.1$ ns, the spatial distribution of the excited $\overline{m_{\mathrm{net}}^z}$ follows the circular shape of the laser spot [7]. As the generated spin waves propagate within the film plane, $\overline{m_{\mathrm{net}}^z}$ in the two cases start to present distinct features. Specifically, the expansion of $\overline{m_{\mathrm{net}}^z}$ keeps isotropic in the absence of magnetic field, but gradually

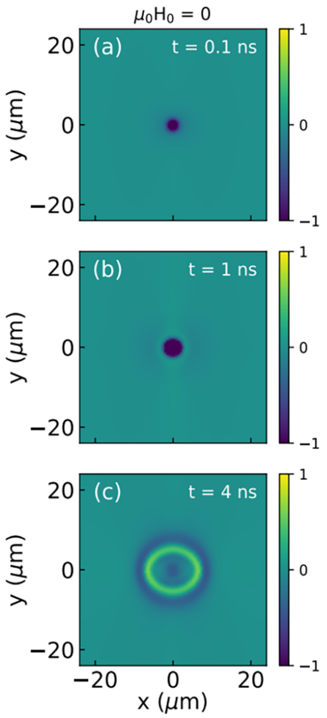

FIG. 9. Evolution of the normalized $\overline{m^z_{\rm net}}$ excited via nonthermal IFE mechanism (a)–(c) without and (d)–(f) with an external magnetic field at $\mu_0 H_0 = 100\,\mathrm{mT}$.

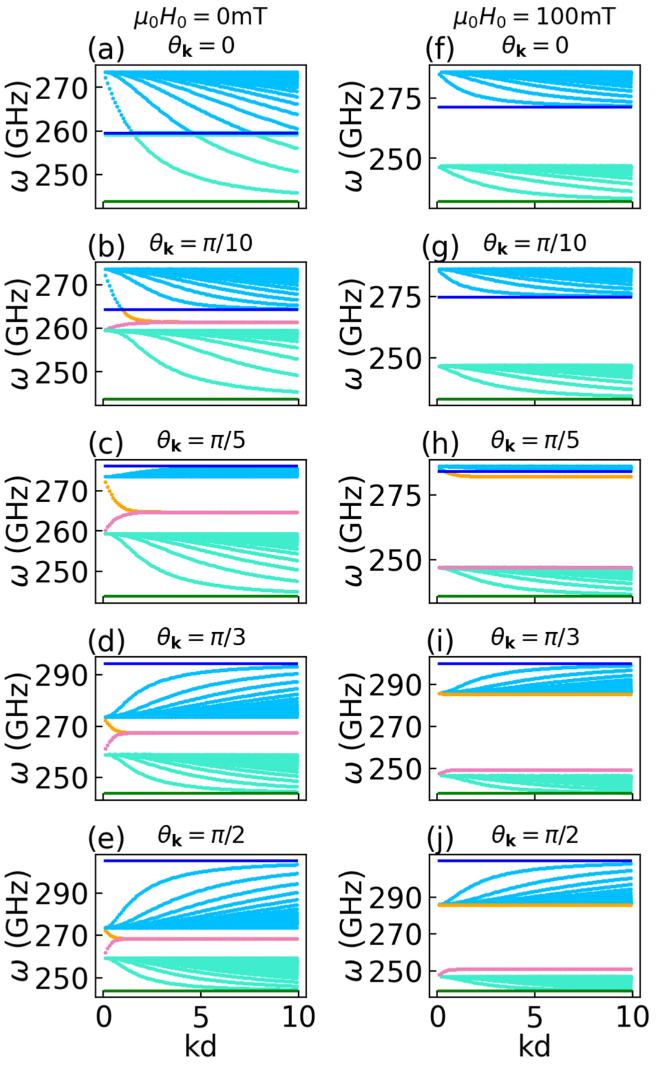

FIG. 10. Spin-wave dispersions in CrSBr film at different wave vectors and magnetic field. The dark blue and dark green solid lines are the high-frequency and low-frequency bulk modes calculated from Eq. (B1). Other symbols are of the same meanings as those in Fig. 3.

becomes anisotropic with an external magnetic field at 100 mT [see Figs. 9(e) and 9(f)]. This reflects the field-induced modification in the spin-wave spectrum and the corresponding wave functions. On the one hand, the magnetic field affects the dispersion of spin waves by increasing the frequency gap between high-frequency and low-frequency modes and altering the group velocity of the spin waves. On the other hand, as discussed above, the symmetry of the wave functions at zero magnetic field prevents the readout of VHs and SL modes from $\overline{m^z_{\rm net}}$. As a consequence, the spin-wave propagation in Figs. 9(a)–9(c) is nearly isotropic within the plane. The inclusion of the magnetic field breaks this relation and activates all modes, including VHs (blue curves in Fig. 10), whose dispersions show a strong angular dependence allowing the anisotropic propagation pattern. A discussion on the role of triaxial anisotropy can be found in Appendix B.

V. SUMMARY AND DISCUSSION

In summary, we studied the laser-induced magnetization dynamics in triaxial antiferromagnet CrSBr film from thermal and nonthermal mechanisms. For the thermal excitation mechanism, we consider the magnetoelastic torque due to the thermally generated shear and pressure pulses of either uniform or standing-wave profiles along the thickness direction. The pressure stress is found to be able to excite magnetization dynamics regardless of the value of external magnetic field, while shear stress can be relevant only when one applies an in-plane magnetic field to modify the symmetry of wave functions or introduce a standing-wave stress in the thickness direction to activate the dark modes with antisymmetric profile of Néel density. Interestingly, the spatial distribution of the excited dynamical magnetization induced by nonuniform shear stress at zero magnetic field exhibits a quadrupolar characteristic, which is in sharp difference from the typical dipolar shape in ferromagnet from the same mechanism. The inclusion of a large magnetic field can change the quadrupolar feature back to the dipolar characteristic. For the nonthermal excitation, the spatial propagation of the excited spin wave is also affected by the magnetic field, which can be understood from the changes in the symmetry and dispersion of the spin waves.

It is also noteworthy that the presence of defects may introduce some additional localized modes [30] or influence the local Heisenberg exchange coupling [42],which may affect the magnetic response but can be safely neglected here because the intensity of such effects is found to be rather weak, and more importantly the size of the defects is typically in the nanometer scale, much smaller than the wavelength of spin wave studied in our present paper.

Finally, we would like to point out that the calculation with a uniaxial anisotropy was also performed, where the results from the thermal excitation were quite similar to those of the triaxial anisotropy presented here, owing to the consistent properties of wave-function symmetry. In nonthermal excitation, the dynamics is determined solely by the properties of the spin waves and hence becomes very sensitive to the magnetic parameters. The evolution of the spatial patterns then rely on the magnetic anisotropy. From applications, ultrafast magnetization dynamics induced by laser can be beneficial for, e.g., ultrafast magnetic storage devices and magneto-optical devices. As previous related studies have been performed mainly in ferromagnets, our paper reveals the possibilities to use antiferromagnets instead, which have many well-known advantages, such as the higher operation speed and the absence of stray field.

ACKNOWLEDGMENTS

This work is supported by the National Natural Science Foundation of China (Grants No. 11974047 and No.12374100) and the Fundamental Research Funds for the Central Universities.

APPENDIX A: COEFFICIENTS IN CHARACTERISTIC EQUATION AND WAVE FUNCTIONS

In the characteristic equation, i.e., Eq. (4), κ, κ', and ν' are defined as

$$\kappa = \kappa_1 + \kappa_2, \quad \kappa' = \kappa'_1 + \kappa'_2, \quad \nu' = \nu'_1 + \nu'_2, \tag{A1}$$

with the detailed expressions of κ_i, ν_i, κ'_i, and ν'_i being the same as those in Eqs. (6) and (7):

$$\begin{aligned}\kappa_{1/2} = \big[&\big(\omega^2 + \omega_\pm\omega_\mp + \omega_{\text{ex}}^2 \pm \omega_{\text{ex}}\omega'_\mp\big)\omega_{\text{ex}}\\ &\mp\omega_\pm(\omega^2 - \omega_\mp\omega'_\mp)\big]/\mathcal{D},\end{aligned} \tag{A2}$$

$$\begin{aligned}\nu_{1/2} = [&\pm(\omega^2 - \omega_\mp\omega'_\mp)\omega\\ &-(\omega_\pm + \omega'_\mp - \omega_{\text{ex}})\omega\omega_{\text{ex}}]/\mathcal{D},\end{aligned} \tag{A3}$$

$$\begin{aligned}\kappa'_{1/2} = \big[&\big(\omega^2 + \omega'_\pm\omega'_\mp + \omega_{\text{ex}}^2 \pm \omega_{\text{ex}}\omega_\mp\big)\omega_{\text{ex}}\\ &\mp(\omega^2 - \omega_\mp\omega'_\mp)\omega'_\pm\big]/\mathcal{D},\end{aligned} \tag{A4}$$

$$\nu'_{1/2} = \nu_{1/2} \pm 2\omega\omega_{\text{ex}}\omega_{\text{a}}^y/\mathcal{D}. \tag{A5}$$

Here, we define the frequencies

$$\omega_\pm = \omega_H \pm \omega_{\text{a}}^x \pm \omega_{\text{ex}}, \tag{A6}$$

$$\omega'_\pm = \omega_\pm \mp \omega_{\text{a}}^y, \tag{A7}$$

with $\omega_H = \gamma\mu_0 H_0$, $\omega_{\text{ex}} = \gamma\mu_0 H_{\text{ex}}$, and $\omega_{\text{a}}^{x,y} = \gamma\mu_0 H_{\text{a}}^{x,y}$. Here, the effective fields due to exchange interaction and anisotropy are defined as $\mu_0 H_{\text{ex}} = 2\mathcal{J}/M_0$ and $\mu_0 H_{\text{a}}^{x,y} = 2K^{x,y}/M_0$, respectively. The denominator in Eqs. (A2)–(A5) is defined as

$$\begin{aligned}\mathcal{D} = \big[&\big(\omega_H^2 - \omega_0^2 + 2\omega_0'^2 - \omega_{\text{a}}^{y2}\big)\big(\omega_H^2 - \omega_0^2\big)\\ &+\omega^4 - 2\omega^2\big(\omega_H^2 + \omega_0^2 - \omega_0'^2\big)\big]/\omega_M,\end{aligned} \tag{A8}$$

with

$$\omega_0 = \big[\big(2\omega_{\text{ex}} + \omega_{\text{a}}^x\big)\omega_{\text{a}}^x\big]^{1/2}, \tag{A9}$$

$$\omega'_0 = \big[\big(\omega_{\text{ex}} + \omega_{\text{a}}^x\big)\omega_{\text{a}}^y\big]^{1/2}, \tag{A10}$$

and $\omega_M = \gamma\mu_0 M_0$.

APPENDIX B: SPIN WAVE SPECTRUM IN CrSBr

According to Sec. II, the spin-wave modes can be calculated from two combined equations of the demagnetization field $\mathbf{H}_{\text{in}} = \nabla\phi$ and sublattice magnetization $\mathbf{m}_{1(2)}$, i.e., Eqs. (3) from Landau-Lifshitz equation and $\nabla \cdot [M_0(\mathbf{m}_1 + \mathbf{m}_2) + \mathbf{H}_{\text{in}}] = 0$ from Maxwell's equation, under the proper boundary conditions. In the film geometry with a finite thickness, all eigenfrequencies for a given in-plane wave vector $\mathbf{k}$ satisfy the characteristic equation, Eq. (4). Some typical dispersions with material parameters in CrSBr are illustrated in Fig. 10 with different values of $\theta_{\mathbf{k}}$, which is defined as the angle between the wave vector and the Néel vector. We adopted both zero and a finite external magnetic field at 100 mT.

Note that the spin-wave spectrum of the triaxial antiferromagnetic thin film differ from those of uniaxial antiferromagnets like MnF_2 [33] mainly in two aspects. First, the low-frequency volume modes are all degenerate in uniaxial antiferromagnet at zero magnetic field, while this degeneracy is lifted by the triaxial anisotropy. Second, the high-frequency volume modes in uniaxial antiferromagnets always have negative group velocities at any $\theta_{\mathbf{k}}$. In triaxial antiferromagnets, the high-frequency volume modes with small $\theta_{\mathbf{k}}$ still have negative group velocities but those at large $\theta_{\mathbf{k}}$ gain positive group velocities, as shown in Figs. 10(c)–10(e) and 10(h)–10(j).

In the bulk case, the scalar potential can be written as $\phi(\mathbf{r}) = \phi_0 e^{i\mathbf{k}\cdot\mathbf{r}+ik^z z}$ [32], where $\mathbf{k}$ remains defined as the in-plane part of the wave vector and k^z is the z component. By substituting this scalar potential into the two combined equations, we obtain the dispersion relations of the two bulk modes,

$$(\omega_{\text{bulk}}^\pm)^2 = b \pm \sqrt{b^2 - ac}, \tag{B1}$$

in which

$$a = \omega_H^2 - {\omega_0}^2, \tag{B2}$$

$$b = \omega_H^2 + {\omega_0}^2 - {\omega'_0}^2 + \omega_{\text{a}}^x\omega_M \sin^2\theta_{\mathbf{k}}, \tag{B3}$$

$$c = 2{\omega'_0}^2 - \omega_{\text{a}}^{y2} - 2\big(\omega_{\text{a}}^x + \omega_{\text{a}}^y\big)\omega_M \sin^2\theta_{\mathbf{k}} + a. \tag{B4}$$

These bulk dispersions with different $\theta_{\mathbf{k}}$ are plotted as the dark blue and dark green solid lines in Fig. 10.

---

[1] E. Beaurepaire, J.-C. Merle, A. Daunois, and J.-Y. Bigot, Phys. Rev. Lett. **76**, 4250 (1996).

[2] K. Yamaguchi, M. Nakajima, and T. Suemoto, Phys. Rev. Lett. **105**, 237201 (2010).

[3] T. Kampfrath, A. Sell, G. Klatt, A. Pashkin, S. Mäehrlein, T. Dekorsy, M. Wolf, M. Fiebig, A. Leitenstorfer, and R. Huber, Nat. Photon. **5**, 31 (2011).

[4] J. R. Hortensius, D. Afanasiev, M. Matthiesen, R. Leenders, R. Citro, A. V. Kimel, R. V. Mikhaylovskiy, B. A. Ivanov, and A. D. Caviglia, Nat. Phys. **17**, 1001 (2021).

[5] A. V. Kimel, A. Kirilyuk, P. A. Usachev, R. V. Pisarev, A. M. Balbashov, and Th. Rasing, Nature (London) **435**, 655 (2005).

[6] T. Satoh, S.-J. Cho, R. Iida, T. Shimura, K. Kuroda, H. Ueda, Y. Ueda, B. A. Ivanov, F. Nori, and M. Fiebig, Phys. Rev. Lett. **105**, 077402 (2010).

[7] T. Satoh, Y. Terui, R. Moriya, B. A. Ivanov, K. Ando, E. Saitoh, T. Shimura, and K. Kuroda, Nat. Photon. **6**, 662 (2012).

[8] A. Ben-Amar Baranga, R. Battesti, M. Fouché, C. Rizzo, and G. L. J. A. Rikken, Europhys. Lett. **94**, 44005 (2011).

[9] A. V. Kimel, A. Kirilyuk, A. Tsvetkov, R. V. Pisarev, and Th. Rasing, Nature (London) **429**, 850 (2004).

[10] A. V. Kimel, C. D. Stanciu, P. A. Usachev, R. V. Pisarev, V. N. Gridnev, A. Kirilyuk, and Th. Rasing, Phys. Rev. B **74**, 060403(R) (2006).

[11] J. A. de Jong, A. V. Kimel, R. V. Pisarev, A. Kirilyuk, and Th. Rasing, Phys. Rev. B **84**, 104421 (2011).

[12] N. Ogawa, W. Koshibae, A. J. Beekman, N. Nagaosa, M. Kubota, M. Kawasaki, and Y. Tokura, Proc. Natl. Acad. Sci. USA **112**, 8977 (2015).

[13] Y. Hashimoto, S. Daimon, R. Iguchi, Y. Oikawa, K. Shen, K. Sato, D. Bossini, Y. Tabuchi, T. Satoh, B. Hillebrands, G. E. W. Bauer, T. H. Johansen, A. Kirilyuk, Th. Rasing, and E. Saitoh, Nat. Commun. **8**, 15859 (2017).

[14] J. Li, C. B. Wilson, R. Cheng, M. Lohmann, M. Kavand, W. Yuan, M. Aldosary, N. Agladze, P. Wei, M. S. Sherwin, and J. Shi, Nature (London) **578**, 70 (2020).

[15] P. Vaidya, S. A. Morley, J. van Tol, Y. Liu, R. Cheng, A. Brataas, D. Lederman, and E. del Barco, Science **368**, 160 (2020).

[16] T. Hioki, Y. Hashimoto, and E. Saitoh, Commun. Phys. **3**, 188 (2020).

[17] D.-L. Zhang, J. Zhu, T. Qu, D. M. Lattery, R. H. Victora, X. Wang, and J.-P. Wang, Sci. Adv. **6**, eabb4607 (2020).

[18] T. Hioki, Y. Hashimoto, and E. Saitoh, Commun. Phys. **5**, 115 (2022).

[19] M. Gidding, T. Janssen, C. S. Davies, and A. Kirilyuk, Nat. Commun. **14**, 2208 (2023).

[20] K. Shen and G. E. W. Bauer, Phys. Rev. Lett. **115**, 197201 (2015).

[21] K. Shen and G. E. W. Bauer, J. Phys. D: Appl. Phys. **51**, 224008 (2018).

[22] Y. Hashimoto, D. Bossini, T. H. Johansen, E. Saitoh, A. Kirilyuk, and Th. Rasing, Phys. Rev. B **97**, 140404(R) (2018).

[23] T. Hioki, Y. Hashimoto, T. H. Johansen, and E. Saitoh, Phys. Rev. Appl. **11**, 061007(R) (2019).

[24] Y. J. Bae, J. Wang, A. Scheie, J. Xu, D. G. Chica, G. M. Diederich, J. Cenker, M. E. Ziebel, Y. Bai, H. Ren, C. R. Dean, M. Delor, X. Xu, X. Roy, A. D. Kent, and X. Zhu, Nature (London) **609**, 282 (2022).

[25] Y. Sun, F. Meng, C. Lee, A. Soll, H. Zhang, R. Ramesh, J. Yao, Z. Sofer, and J. Orenstein, Nat. Phys. **20**, 794 (2024).

[26] T. Janssen, M. Gidding, C. S. Davies, A. V. Kimel, and A. Kirilyuk, Phys. Rev. B **108**, L140405 (2023).

[27] Y. J. Bae, T. Handa, Y. Dai, J. Wang, H. Liu, A. Scheie, D. G. Chica, M. E. Ziebel, A. D. Kent, X. Xu, K. Shen, X. Roy, and X. Zhu, Phys. Rev. B **109**, 104401 (2024).

[28] X. Xu, X. Wang, P. Chang, X. Chen, L. Guan, and J. Tao, J. Phys. Chem. C **126**, 10574 (2022).

[29] A. Pawbake, T. Pelini, N. P. Wilson, K. Mosina, Z. Sofer, R. Heid, and C. Faugeras, Phys. Rev. B **107**, 075421 (2023).

[30] K. Torres, A. Kuc, L. Maschio, T. Pham, K. Reidy, L. Dekanovsky, Z. Sofer, F. M. Ross, and J. Klein, Adv. Funct. Mater. **33**, 2211366 (2023).

[31] R. Damon and J. Eshbach, J. Phys. Chem. Solids **19**, 308 (1961).

[32] R. E. Camley, Phys. Rev. Lett. **45**, 283 (1980).

[33] J. Liu, L. Wang, and K. Shen, Phys. Rev. Res. **2**, 023282 (2020).

[34] R. Verba, G. Melkov, V. Tiberkevich, and A. Slavin, Phys. Rev. B **85**, 014427 (2012).

[35] H. T. Simensen, R. E. Troncoso, A. Kamra, and A. Brataas, Phys. Rev. B **99**, 064421 (2019).

[36] G. Benedek, J. Ellis, A. Reichmuth, P. Ruggerone, H. Schief, and J. P. Toennies, Phys. Rev. Lett. **69**, 2951 (1992).

[37] A. Link, R. Sooryakumar, R. S. Bandhu, and G. A. Antonelli, J. Appl. Phys. **100**, 013507 (2006).

[38] S. Ge, X. Liu, X. Qiao, Q. Wang, Z. Xu, J. Qiu, P.-H. Tan, J. Zhao, and D. Sun, Sci. Rep. **4**, 5722 (2014).

[39] J. P. van der Ziel, P. S. Pershan, and L. D. Malmstrom, Phys. Rev. Lett. **15**, 190 (1965).

[40] P. S. Pershan, J. P. van der Ziel, and L. D. Malmstrom, Phys. Rev. **143**, 574 (1966).

[41] L. Talirz, S. Kumbhar, E. Passaro, A. V. Yakutovich, V. Granata, F. Gargiulo, M. Borelli, M. Uhrin, S. P. Huber, S. Zoupanos *et al.*, Sci. Data **7**, 299 (2020).

[42] J. Klein, Z. Song, B. Pingault, F. Dirnberger, H. Chi, J. B. Curtis, R. Dana, R. Bushati, J. Quan, L. Dekanovsky, Z. Sofer, A. Alu, V. M. Menon, J. S. Moodera, M. Loncar, P. Narang, and F. M. Ross, ACS Nano **17**, 288 (2023).